Supplementary Information

Efficient AC electrothermal flow (ACET) on-chip for enhanced immunoassays

Muaz Draz,*[a] Kevin Uning,[a] Diego Dupouy, [b] and Martin A. M. Gijs [a]

a: Laboratory of Microsystems, Ecole Polytechnique Fédérale de Lausanne (EPFL), CH-1015 Lausanne, Switzerland

b: Lunaphore Technologies, CH-1131 Tolochenaz, Switzerland
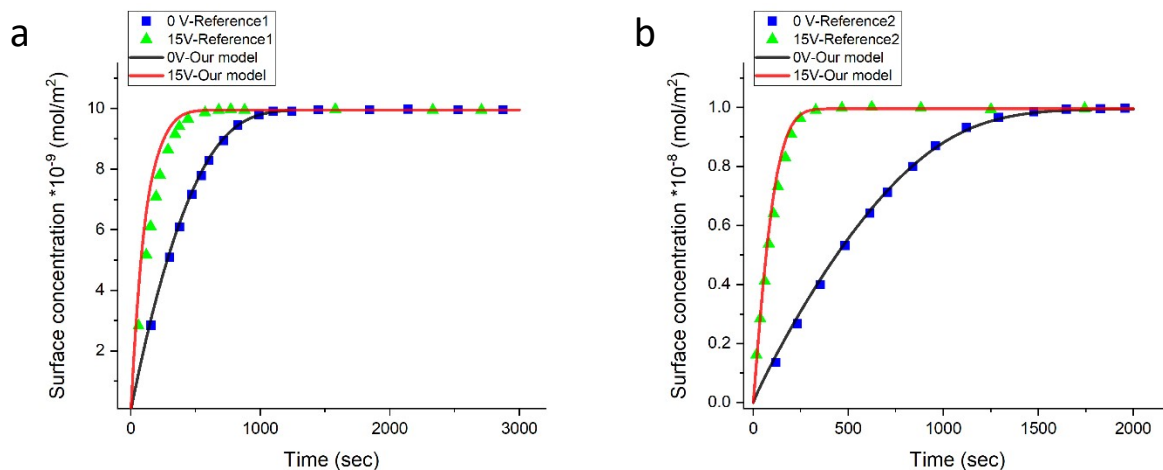
Supplementary Figures

Figure S1 Benchmarking of the numerical simulation model used in the current work with simulations from the published literature. (a) and (b) show the theoretical enhancement of the surface reactions with the AC electrothermal microfluidic mixing using our model and compared with the results of the listed literature.

Here we validated our ACET simulation model against the results published by two groups. Figure S1a shows the validation of our model against the system design of Huang K.R. et al. [1] with electrodes length of 100 μm. Figure S1b shows the validation against the system design of Yang C.K. et al.[2] with the reacting surface located at (x=281 and y=133) within the 2D simulation. In both cases, we were able to replicate their results with a large agreement between their published work and our model results.

Here, we validated our simulation model for the surface binding reaction against the experiment done by Berthier J. et al.,[3] in which they monitored the fluorescent signal of different DNA strands hybridizing to surface-immobilized and complementary DNA sequences. The flow is turned on for 50 minutes, then it is stopped for 310 minutes, and it is again turned on for the rest of the experimental time which explains the curve shape after 21600 seconds. The average flow velocity is 1 mm/s (10 μl/min) and the dimensions of the microchamber are $10 \times 10 \times 1$ mm^3. The results show a large agreement between the experiment and the simulation modeling results for the surface-based immunoassays. This indicates the accuracy of our numerical simulation, allowing us to fit also other parameters of the surface-based immunoassay experiments, such as reagents concentrations, and association constants.
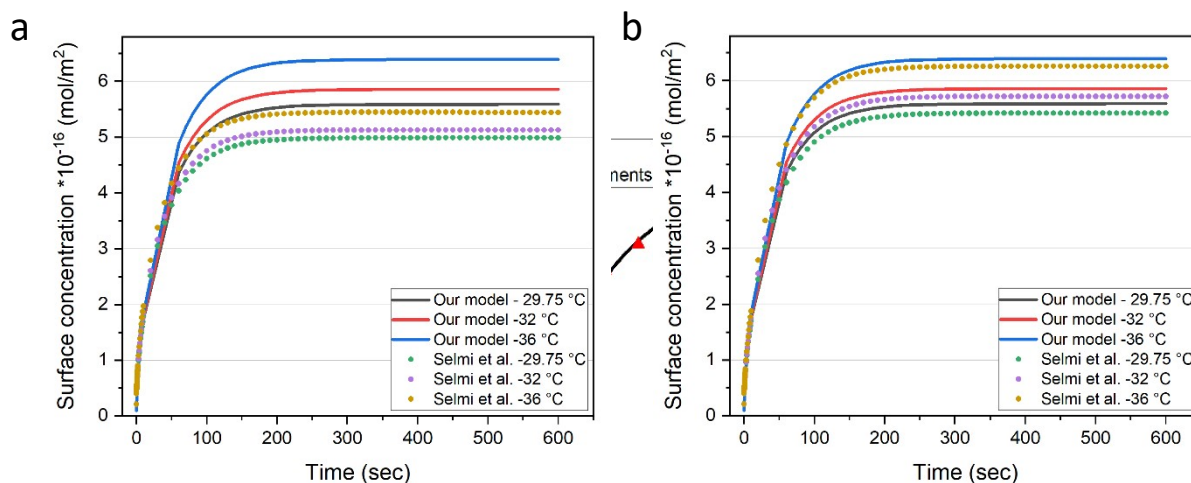

Figure S3 Comparison of the numerical simulation model used in the current work with electrode design from the published literature. (a) and (b) show the theoretical enhancement of the surface reactions with the AC electrothermal microfluidic mixing, using our model compared with the M. Selmi et al. (4) ACET design with parallel electrodes at their reported gap between the electrodes (a) and for a similar gap as in our design (b). Both designs were compared at several volume temperatures (29.75, 32, 36 °C).

Time (sec)

Figure S2 Validation of our simulation model for the surface-based reaction against the published experimental results of DNA fluorescent hybridization.

Here, to validate further our numerical model, we compare our small in-plane design against the model with parallel electrodes design proposed by M. Selmi et al.,[4] at their reported gap between the electrodes of 5 µm (Figure S3a) and a similar gap as in our design of 85 µm (Figure S3b). In both cases, our design shows higher enhancement in the surface reaction (mol/m^2) at different average temperatures. We believe this is mainly due to the larger in-plane mixing capability of the in-plane design.
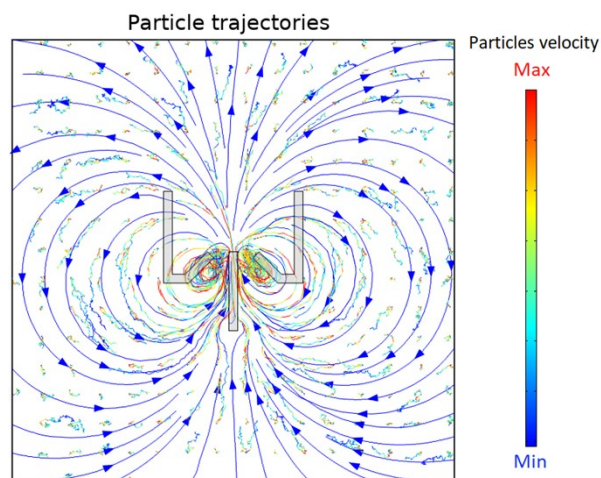

Figure S4 Simulation of particles tracing. 20 nm nanoparticles' trajectories are shown in response to the ACET fluid motion (blue lines with arrows) after 60 seconds of applying the ACET voltage.

Here we show how nanoparticles (20 nm radius), in resemblance to the small biochemical reagents, would react to the ACET fluid motion. These simulations consider the effect of the fluid drag forces on the microparticles by using the Stokes drag law, the effect of the temperature on the Brownian motion and the fluid dynamic viscosity, and finally the gravitational forces. It is clear from the particle's traces in Figure S4 that the microparticles inside the chamber follow the same direction as the fluid motion (blue lines/arrows) in response to the applied ACET voltage. Moreover, it can be seen from the concentrated (yellow to red) tracing lines at the center, that the microparticles located at that location will experience the largest ACET forces. This can be explained by the high electric field intensity and thus the maximum fluid velocity at that location.
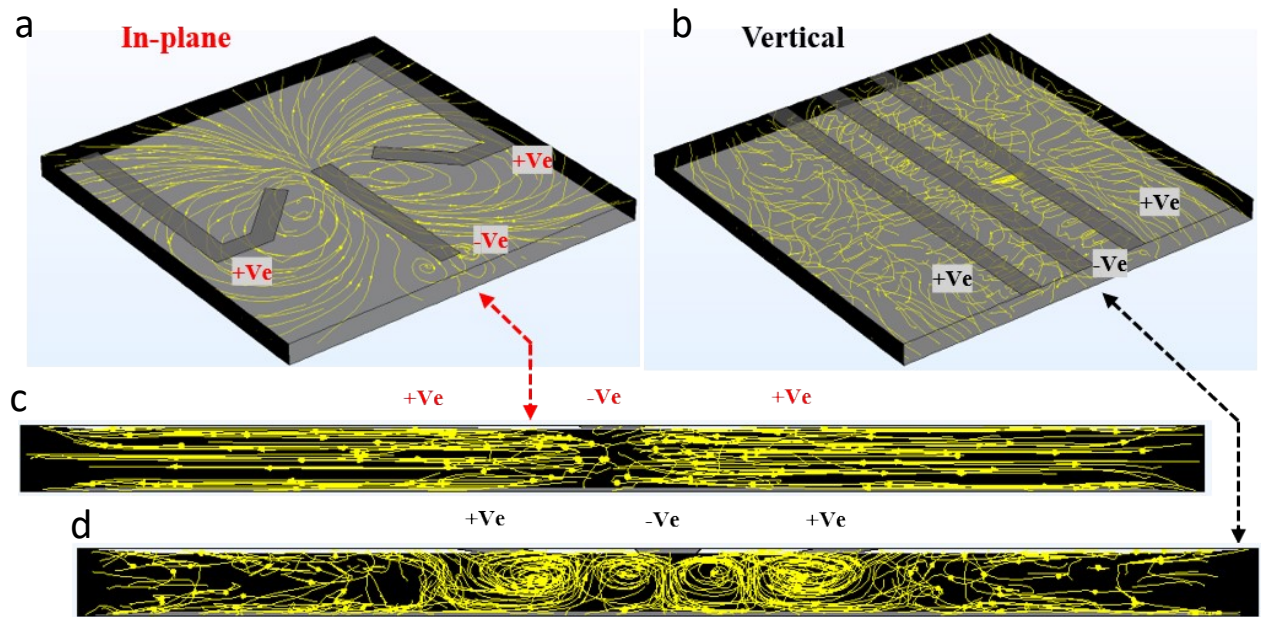
Figure S5 Numerical simulation comparison of the fluidic streamlines of the in-plane and vertical vortices designs. (a) 3D view and (c) the corresponding side view of the fluidic streamlines generated by the ACET actuation of the in-plane vortex design. (b) 3D view and (d) the corresponding side view of the fluidic streamlines generated by the ACET actuation of the vertical vortex design. Both designs have 50 µm wide electrodes and 85 µm interspacing gap between each of the two side electrodes and the middle electrode.

Here we show how the ACET actuation of the in-plane (Figure S5a) and vertical (Figure S5b) vortex designs generate different fluidic streamlines. The in-plane design vortex generates in-plane fluidic motion, while the traditional vertical design with parallel electrodes generates a local vertical vortex fluidic motion. This is further confirmed by Figures S5c and S5d, which show the fluidic streamlines from the corresponding side view of the microfluidic chamber for the in-plane and vertical vortex design, respectively. It can be seen clearly that the in-plane design is capable of inducing a large-scale fluidic motion across the width of the chamber. The vertical design shows two vertical vortices mainly localized at the center of the chamber between each of the two side electrodes and the middle electrode.
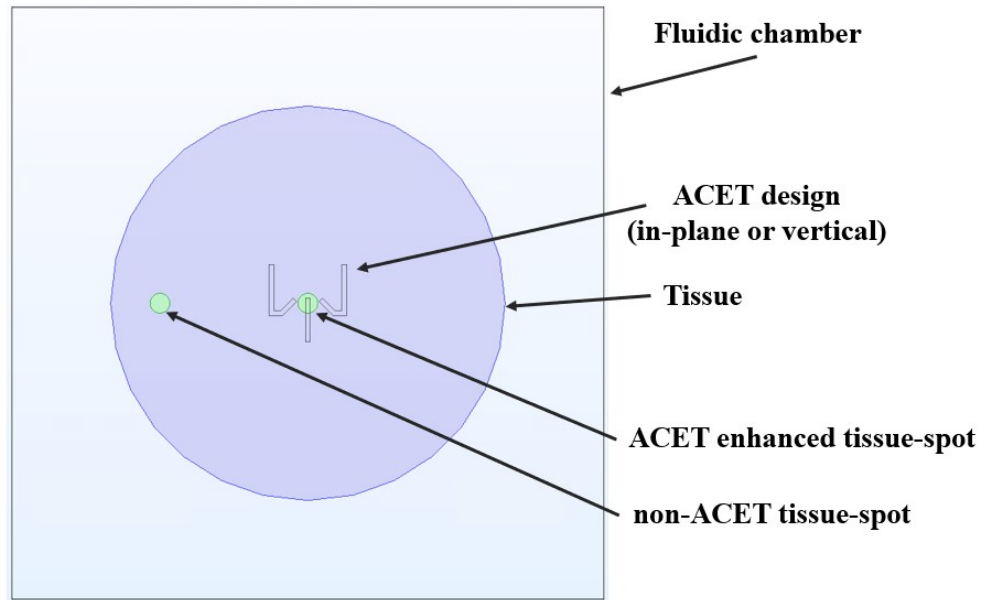
Figure S6 Schematic representation of the microfluidic chamber with the cell pellet or tissue section and ACET mixing design used for the experimental validation of the ACET-enhanced immunostaining. The ACET mixing design (shown here is the in-plane design, but similarly a vertical electrode design can be imagined) with the BT-474 breast cancer cell pellet (tissue) located at the bottom of the chamber. Two spots were considered for the subsequent analysis, namely a ACET-enhanced tissue spot for the area located below the ACET designs, and another spot (non-ACET tissue spot) located at least 1~2 mm far away.
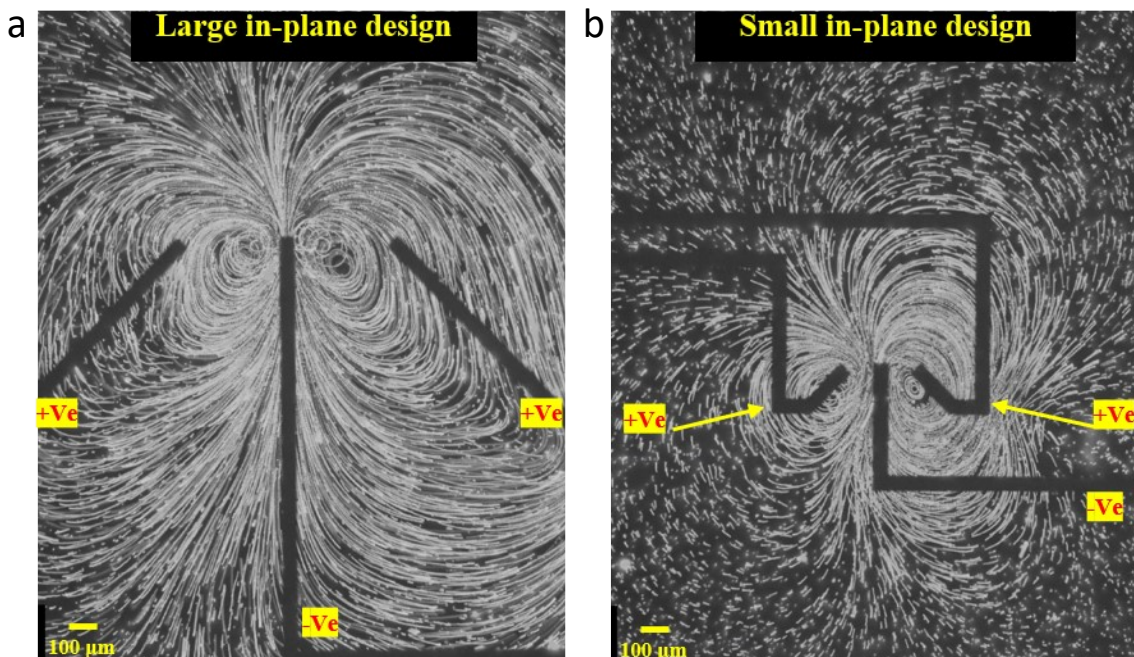
Figure S7 The in-plane ACET motion obtained by the large (a) and small (a) in-plane designs. The figures show the superimposed images of a time sequence of fluorescent microparticles moving along with the ACET in-plane vortices. A similar number of frames (300 frames) were used to generate the images.

Here we show the different ACET mixing coverage areas by the large (Figure S7a) and small (Figure S7b) in-plane designs, obtained after superimposing a similar number of frames and while actuating both designs with the maximum possible ACET power (that at which, it was still safer to avoid bubbles and electrolysis). It shows clearly that the large design can induce ACET in-plane fluid motion over a larger area.
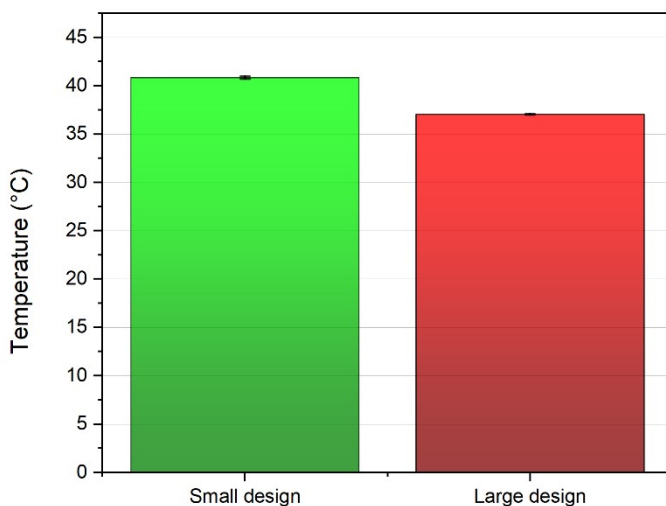

Figure S8 The maximum temperature measured by the thermal IR camera during the ACET actuation of the small and large in-plane designs at 30 Vpp and 1 MHz. Error bars represent the standard deviation (n=4).

Here we show the maximum temperature obtained by the small and large in-plane designs at 30 Vpp and with fluid conductivity of 1.5 S/m. The large design shows a lower maximum temperature than the small design. This is partially due to the increased gap between the two side and middle electrodes (340 μm vs 85 μm for the small in-plane design).
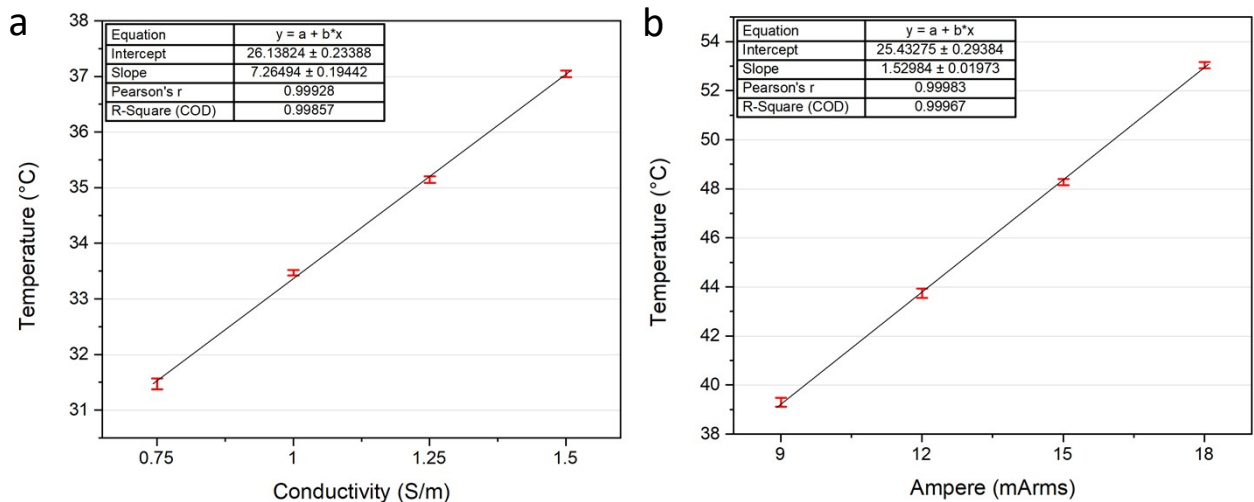
Figure S9 The maximum temperature measured by the thermal IR camera during the ACET actuation of the large in-plane design for (a) different fluid conductivities (S/m) at 30 Vpp 1MHz and (b) different ACET power (electrical current (mArms)) using a fluid conductivity of 1.5 S/m. Error bars represent the standard deviation (n=4).

The large in-plane ACET actuation was tested with several fluids with different electrical conductivities (0.75 to 1.5 s/m) at 30 V_{pp} 1 MHz. The results (Figure S9a) show a linear correlation between the temperature and the conductivity (Pearson's product-moment correlation coefficient= 0.99). Moreover, the maximum obtainable temperature was measured as a function of ACET actuation current (9 to 18 mArms) using the large in-plane design (Figure S9b). The design shows a linear relationship between the ACET current and the achieved temperature (Pearson's product-moment correlation coefficient =0.99). In general, increasing the conductivity of the solution or the current (power) would lead to an increase in the generated ACET forces and the resulting microfluidic mixing. Higher currents than those reported here would then lead to too high temperatures, leading to the generation of bubbles and possibly electrolysis.
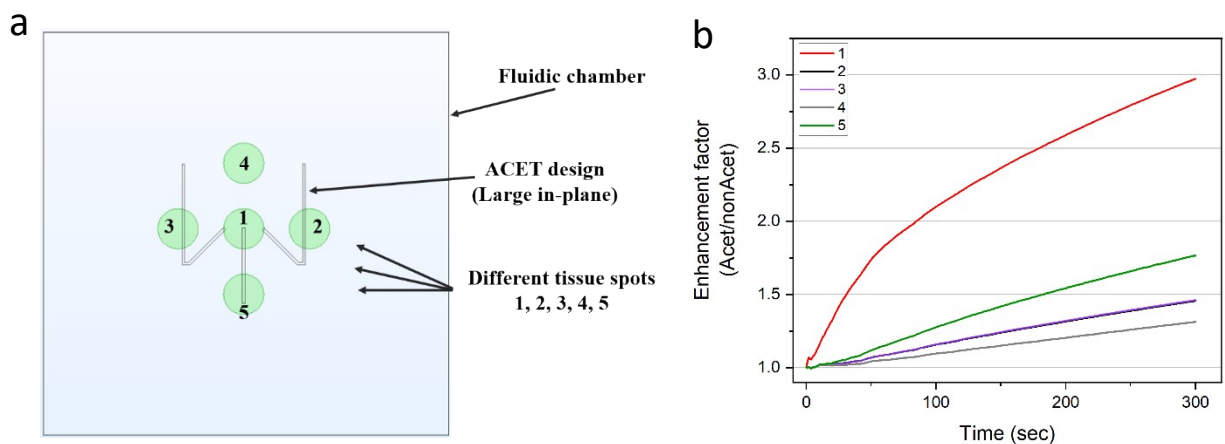

Figure S10 Schematic represention of the microfluidic chamber with the large in-plane design and theoretical simulation of the position-dependent ACET-enhanced surface reaction. (a) The large in-plane electrode design located within a microfluidic chamber and locations used for calculating the ACET-enhanced surface reaction (1: centre, 2: right, 3: left, 4: top, 5: bottom of the design). (b) Enhancement factor for t= 5 minutes of the surface-bound species (25 V_{pp}/0 V_{pp}) for the different surface reaction spots indicated in Figure S10a.

Here we show by numerical simulation the effect of the in-plane design location on the enhanced surface reactions. Figure S10b shows that the area located at the center of the design (1) has the highest enhancement in the surface reaction due to the maximum ACET forces located at the design center. This is further supported by the dense microparticle trajectories located at the design center as seen in the experiment (Figure S7a). The bottom spot (5) shows

a higher enhancement than the right (2) and left (3) and top (4) spots, probably due to the ability of the design to drag and push the fluid from the bottom stronger than from the other locations, resulting in a higher enhancement.
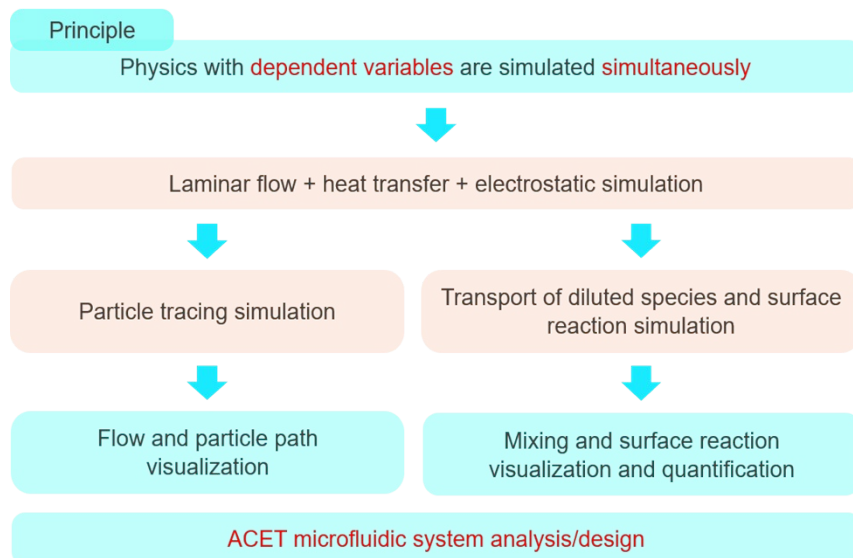

Figure S11 Pipeline of the numerical simulation strategy for solving the laminar flow, heat transfer, electrostatics, particle tracing, transport of diluted species, and surface reaction problems.

Table S1 Values of the numerical simulation variables

Variable	Value	Description
ω	2*π*1e6 [Hz]	Angular frequency of the AC signal
V0_rms	Vpp/(2*sqrt(2))	V_{RMS} (Volt root mean square) of the V_{pp} (Volt peak to peak)
T_0	293.15 [K]	Reference ambient temperature
$\dfrac{1}{\varepsilon}\dfrac{\partial \varepsilon}{\partial T}$	-0.004 [1/K]	Permittivity ratio change per Kelvin
$\dfrac{1}{\sigma}\dfrac{\partial \sigma}{\partial T}$	0.02 [1/K]	Electrical conductivity ratio change per Kelvin
σ	1.5 [S/m]	Solution electrical conductivity
length	15 [mm]	Microfluidic chamber length
width	15 [mm]	Microfluidic chamber width
width_el	50 [um]	Electrode width
gap_el	85 [um]	Gap between electrodes
r_particle	20 [nm]	Particle radius used in the particle tracing study
c_0	1e-6 to 1e-11 [mol/m^3]	Initial analyte concentration
kon	1e3 to 1e5 [m^3/mol/s]	Association reaction constant
Kd	1e-2 [1/s]	Dissociation reaction constant
B0	3.3e-8 [mol/m^2]	Surface target (bioreagent) density

Table S2 Boundary conditions for the numerical simulations

Boundary	Electrical boundary condition	Thermal boundary condition	Fluidic boundary condition	Transport of diluted species (tds) boundary condition	Surface reaction (sr) boundary condition
Top surface	Zero charge[1]	Natural convection[2]	—	—	—
Side walls	Zero charge[1]	Side-wall natural convection[2]	—	—	—
Bottom surface	Zero charge[1]	T_0	—	—	—
Electrode surface	$V_{0,RMS}$	—	Wall, no slip[3]	No flux[5]	—
Counter electrode surface	$-V_{0,RMS}$	—	Wall, no slip[3]	No flux[5]	—
Chamber top surface	—	—	Wall, no slip[3]	No flux[5]	—
Chamber side walls	—	—	Open boundary[4]	Open boundary[6]	—
Chamber bottom surface	—	—	Wall, no slip[3]	No flux[5]	—
Reacting surface	—	—	Wall, no slip[3]	Outward flux due to surface reaction[7]	Surface reaction[8]

1 $\hat{n} \cdot \vec{D} = 0$

2 $q_0 = h(T - T_0)$, where T and T_0 are the temperature and the reference ambient temperature

3 $\vec{u} = \vec{0}$, where u is the fluid velocity

4 $p = 0$, where p is the pressure

5 $-\hat{n} \cdot (\vec{J} + \vec{u}c) = 0$

6 $\begin{cases} -\hat{n} \cdot \vec{J} = 0, & if\ \hat{n} \cdot \vec{u} \geq 0 \\ c = c_0, & if\ \hat{n} \cdot \vec{u} < 0 \end{cases}$, where c is the reagent concentration

7 $\dfrac{\partial [A]}{\partial t} = -\left(k_{on}[A]_{surface}\{[B_0] - [AB]\} - k_d[AB]\right)$

8 $\dfrac{\partial [AB]}{\partial t} = k_{on}[A]_{surface}\{[B_0] - [AB]\} - k_d[AB]$

Supplementary protocols

Immunoassay protocols

Preparation and blocking:

A BT-474 FFPE cell pellet block (Amsbio) was sectioned into 5 µm thick slices and loaded on Superfrost Plus adhesion microscopic slides (Epredia). Before the immunostaining, the cell pellet sections were dewaxed and deparaffinized using the PT module (Epredia) for 1 hour into the Dewax and HIER Buffer H (PH 9) at 102 °C. After that, the slides were kept in TBST (Tris-buffer saline with 0.005% tween-20) until the blocking step.

The slides were then quenched for 2 minutes with Quenching buffer 1x (BU08-L, Lunaphore) diluted into TBS buffer (Tris-buffer saline). The slides were then washed thoroughly with TBST and then incubated for 5 minutes with bovine serum albumin (3%, AURION BSA-c, diluted in staining buffer). Finally, the slides were washed thoroughly with TBST and used for the endogenous biotin-blocking step.

A streptavidin/biotin blocking step was carried out to reduce any nonspecific signal coming from endogenous biotin or streptavidin binding sites present in the cells. The cell sections were incubated with a streptavidin-blocking solution for 15 minutes, then washed with TBS for 3 minutes, and then incubated with the biotin-blocking solution for 15 minutes, followed by 9 minutes of washing with TBS. The streptavidin blocking step would block the endogenous biotin, while the biotin blocking step would block the free binding sites available on the streptavidin molecule. Finally, the slides were kept in TBS till the immunostaining step.

Immunostaining:

The slides were then loaded into the microfluidic system shown in Figure 1 and the following bioassay protocol was used for all the slides. The BT474 cell sections were first incubated with a Her2/Neu (EP3) rabbit monoclonal primary antibody (237R-25-ASR, Cell marque) diluted into TBST for 2 minutes. The slides were then washed thoroughly with TBST and subsequently incubated for 2 minutes with a Goat anti-rabbit IgG (H+L) Highly Cross-Adsorbed secondary antibody-Biotin (A16114, Thermofisher). The primary and the secondary antibodies were diluted 1:100 into a 1.5 S/m multi-staining buffer, and the ACET actuation was applied during their incubation. Dapi (62248, Thermofisher) was diluted to 1:1000 with the secondary antibody and used for nuclear counterstaining. All the reagents handling (dispensing into the microfluidic chamber and fluid aspiration) and flow rate control were done with an automatic pressure pumping system integrated with the experimental setup.

After washing thoroughly with TBST, the biotin conjugation on the secondary antibody allowed for the final step of binding the streptavidin molecules conjugated with the Alexa Fluor™ 647 label (S32357, Thermofisher). The Streptavidin-Alexa Fluor™ 647 label was diluted 1:200 into TBST and incubated for 2 minutes without applying any ACET actuation with the small in-plane design and with ACET actuation for the large in-plane design. The slides were then washed thoroughly with TBST and unloaded from the microfluidic stainer system.

Fluorescence microscopic imaging and analysis:

Finally, the slides were mounted with coverslips using the SlowFade Gold mounting medium (S36936, Invitrogen) for microscopic imaging. The slides were imaged using the PANNORAMIC MIDI II automatic slide scanner (3DHISTECH) with SOLA Light illumination engine (Lumencor). The focal level was adjusted for each imaging tile, and the whole cell-pellet section was imaged using a 20x (NA 0.8) objective. The exposure time was adjusted for each slide to avoid over- or under-exposure of the cell sections, and the different exposure times were considered during the image analysis. A similar region-of-interest (ROI) size for all the images was exported and analyzed using a CellProfiler (4.2.1) pipeline. Briefly, an adaptive Otsu thresholding was used to classify the her2 signal for each cell and assigned it as Signal (S), and the inverse of the mask was used as Background (B) to account for any fluorescent signal coming from outside the cells. For the visualization of ACET fluidic streamlines, TetraSpeck Microspheres 1.0 µm (T7282, Thermofisher) were diluted in TBST and used for observing the ACET fluidic motion.

Infrared thermal imaging:

An infrared thermal camera (PI 640i, Optris), was used for the thermal monitoring at a frequency of 31 Hz during the ACET experiments and for the large ACET in-plane design characterization at different fluid electrical conductivities and different ACET power.

Fabrication of the micro-electrodes

Preparation and resist coating:

High-precision 1.5H (18×18 mm2) microscopic coverslips (LH22.1, Carl Roth) were used for the electrode's lift-off microfabrication process. The coverslips were first cleaned for 10 minutes into IPA (isopropyl alcohol) and dried using nitrogen air. After that, the coverslips were put on a hotplate at 100 C° for 3 minutes to have a dry surface. The coverslips were then coated with LOR-5A (Kayakuam) as a sacrificial resist at 2500 rpm and baked at 170 °C for 4:10 minutes. Later, the coverslips were coated with AZ-1512 HS (Microchemicals) at 2250 rpm and baked at 100 °C for 1.30 minutes. The slides were then left for 15 minutes in a humidity-controlled environment.

Laser exposure and resist development:

The coverslips were then exposed using the Maskless Aligner MLA 150 (Heidelberg Instruments) with 80 mJ/cm^2 using an h-line (405 nm) laser source. The coated coverslips were then developed using AZ-726 MIF (Microchemicals) for 1:10 minutes and thoroughly washed with deionized water.

Lift-off evaporation and resist stripping:

The coverslips were then plasma-cleaned with a Tepla 300 system (PVA TePla AG) for 30 seconds at 200 watts. We found this step to be essential to remove any contaminants left on the patterned surface that otherwise can lead to an unsuccessful lift-off process. Then, the metal evaporation was done by loading the coverslips on copper thermal plates to avoid temperature rise. Hereafter, the coverslips were coated with 30 nm of chromium (adhesion layer) followed by 200 nm of platinum. After that, the resist stripping process was done by sonicating the coverslips for 5 minutes into 1165 Remover (Microresist) and then sonicating for 10 minutes into IPA. The electrodes are 50 μm wide with an 85 μm gap distance gap. Finally, the coverslips were mounted on the staining chip (Figure 1) using UV curable glue and wired as explained.

Supplementary Videos

Video S1: Experimental results of the fluidic motion generated by the new small in-plane ACET design using 1 μm fluorescent microparticles diluted in 1.5 S/m buffer solution.

Video S2: Experimental results of the fluidic motion generated by the new large in-plane ACET design using several sizes of fluorescent microparticles (2, 4, 4.96, 8.87, 10.14 μm) diluted in 1.5 S/m buffer solution.

References

1. Huang KR, Chang JS. Three dimensional simulation on binding efficiency of immunoassay for a biosensor with applying electrothermal effect. Heat Mass Transfer. 2013;49:1647–58.

2. Yang CK, Chang JS, Chao SD, Wu KC. Two dimensional simulation on immunoassay for a biosensor with applying electrothermal effect. Appl Phys Lett. 2007;91:113904.

3. Berthier J, Silberzan P. Microfluidics for Biotechnology, Second Edition [Internet]. [cited 2022 Jun 15]. Available from: https://ieeexplore.ieee.org/document/9100092

4. Selmi M, Khemiri R, Echouchene F, Belmabrouk H. Electrothermal effect on the immunoassay in a microchannel of a biosensor with asymmetrical interdigitated electrodes. Applied Thermal Engineering. 2016;105:77–84.